Joint Phase-Screen Estimation in Airborne Multibaseline SAR Tomography Data Processing

Pasquale Imperatore, *Senior Member, IEEE*, and Gianfranco Fornaro, *Fellow, IEEE*

***Abstract*— Airborne interferometric data is typically affected by phase distortions originated from subwavelength residual positioning uncertainties (phase screen) when acquired along different tracks. Available methods estimate the phase screen affecting stacks of multibaseline acquisitions, mainly by exploiting single interfograms separately. A novel method for the joint estimation of the multibaseline phase screens is proposed. The results of the implemented phase calibration are analyzed via a tomographic inversion, allowing to obtain a 3-D imaging estimating the vertical characteristics of the scene scattering. Specifically, we processed the multibaseline, fully polarized P-band synthetic aperture radar (SAR) data collected during the AfriSAR campaign in July 2015 over the Lopé tropical forests in Gabon, West Africa. Validation of the 3-D imaging results, supported by reference LiDAR (NASA LVIS) data, allowed demonstrating that the proposed joint estimation method overcomes the classical disjoint estimation solutions.**

***Index Terms*— Airborne, motion compensation, phase calibration, phase screen, SAR tomography, synthetic aperture radar (SAR).**

I. Introduction

SYNTHETIC aperture radar (SAR) tomography (TomoSAR) is an important technique based on the use of multibaseline (MB) SAR data to obtain information on the 3-D structure and distribution of volumetric scatters [1], [2], [3], [4]. The capabilities of the technique have been demonstrated in the 3-D reconstruction of urban and forest areas, in both spaceborne and airborne scenarios [5], [6], [7], [8], [9], [10], [11], [12].

The monitoring of forest vertical structure is crucial in the understanding of the dynamics of forest ecosystems, and how they are affected by natural and anthropogenic processes. Remarkably, biomes covering roughly 38% of Earth's vegetated surface area, containing 81% of the estimated total terrestrial phytomass, exhibit biomass densities surpassing the backscattering saturation limit, exceeding 100 tons/ha for P-band (around 450 MHz) [13]. The saturation effect has been largely investigated [14], thus motivating the introduction of tomographic SAR approaches.

Multibaseline SAR systems with varying spatial resolutions have demonstrated significant promise in the study of 3-D forest structures. Nonetheless, the reflectivity interpretation in terms of scattering phenomena from complex 3-D structures, especially in the case of forest vertical structure, is still in its infancy. In particular, the analysis of multichannel signals for forest characterization is a complex task since many factors (e.g., canopy structure, soil moisture and plant water content, observation direction, topographic relief, multiple scattering, etc.) considerably affect the backscattering properties represented in the different observations to be combined.

With reference to the specific problem of MB 3-D SAR focusing considered in this work, the presence of phase artifacts (commonly referred to as phase screens or phase errors) is critical for TomoSAR reflectivity reconstruction, especially in the airborne case [8], [15].

In recent years, airborne SAR systems have been employed for monitoring and mapping biomass in forest regions at a regional scale; P- and L-band sensors have been explored to characterize the 3-D structure of terrain and vegetation [2], [16], [17], [18]. Multipolarimetric P-band SAR tomography for mapping ground topography has been investigated in [19] by relying on the algebraic synthesis technique adopted in [20].

Two main unavoidable sources causing phase artifacts can be distinguished: residual track positioning uncertainties and atmospheric propagation delay variations. If not properly compensated for, these phase artifacts critically cause defocusing and blurring in achieved tomographic profiles.

In the case of MB satellite data, atmospheric propagation delay effects might be relatively large, while baseline uncertainties are not critical due to the stability of the platform [6], [7], [21]. Conversely, airborne SAR systems are highly affected by platform instabilities [8]. Motion errors may even lead to defocusing if not properly accounted during the SAR image formation process [22], [23]. In any case, integrating Inertial Motion Units (IMUs) measurements with autofocusing techniques can hardly lead to compensation reaching the subwavelength scale accuracy [8]. Subwavelength

Manuscript received 31 January 2024; revised 22 May 2024 and 22 July 2024; accepted 12 August 2024. Date of publication 19 August 2024; date of current version 16 September 2024. This work was supported in part by Italian Space Agency (ASI), through the Project MEFISTO "Metodi di Elaborazione di dati SAR multi-Frequenza per Il monitoraggio del disseSTO idrogeologico"; in part by European Union through Italian National Recovery and Resilience Plan (NRRP) of Next Generation EU, partnership on "Telecommunications of the Future" (PE0000001 - program RESTART), and by the Project Space It Up funded by ASI and MUR – Contract n. 2024-5-E.0 - CUP n. I53D24000060005; AfriSAR campaign data were provided by the European Space Agency (ESA) through the Science Proposal 69872. *(Corresponding author: Gianfranco Fornaro.)*

The authors are with the National Research Council (CNR), Institute for Electromagnetic Sensing of the Environment (IREA), 80124 Naples, Italy (e-mail: imperatore.p@irea.cnr.it; fornaro.g@irea.cnr.it).

Digital Object Identifier 10.1109/TGRS.2024.3446186

inaccuracies in the sensor position during the data acquisitions have a critical impact on the coherent processing of airborne MB data [8], [9].

The focus of this work is on the phase compensation of PHase Screen (PHS), originated from the instability of the aircraft affecting the tomographic processing of airborne MB data, for the application to 3-D imaging in forested areas. Different approaches have been proposed in the literature to cope with this problem. In [8], a widely used approach is proposed for calibrating tomographic data. The strategy is in this case based on the so-called double (target and sensor) localization, where the sensor position errors are responsible for the phase disturbances in the data stack. In this case, a geometric space-variant model for the phase distortion is adopted. Conversely, a pixel-by-pixel entropy minimization-based profile reconstruction was investigated in [24] and [25]. In [25], phase calibration is performed by optimizing the entropy of the vertical profile with a zero phase derivative constraint, in order to solve the problem of uncontrollable vertical shifts in the tomographic focusing.

In this work, we propose an improvement to the method developed in [8] for compensating phase distortion in MB airborne SAR data. In [8], the estimation is carried out separately for each interferogram (disjoint estimation) by modeling the range variation of the phase distortion for each azimuth platform position. Differently, our proposed approach performs an optimization aimed at jointly estimating the corrections for all the available passes [26]. The proposed method inherently handles the presence of redundancy in the generation of the interferogram stack from the MB SAR data, thereby ensuring higher robustness.

The validity of the method is assessed by using a real MB dataset acquired by a P-band SAR system over a tropical forest in Gabon and reference NASA LVIS LiDAR data [27]. Furthermore, the results of the proposed method are compared with those obtained with the classical disjoint approach.

The work is organized as follows. Section II introduces the formulation of the problem, with emphasis on the PHS estimation. The proposed method is discussed in Section III. Experimental results are provided in Section IV. Section V provides further discussions on the adopted assumptions and choices. Finally, Section VI provides the conclusions.

II. Problem Formulation

The problem formulation is organized in three different parts: tomographic formulation for 3-D imaging in the presence of phase errors, the network formulation for the generation of the interferograms (observables), and the space-variant PHS model.

A. Three-Dimensional TomoSAR Imaging in the Presence of Phase Errors

Let us consider N single-look complex (SLC) SAR images acquired at different times along distinct and nonuniformly spaced tracks/orbits over the same target area. We indicate with M the number of interferograms that are generated, for calibration purposes, from the N images, according to the adopted

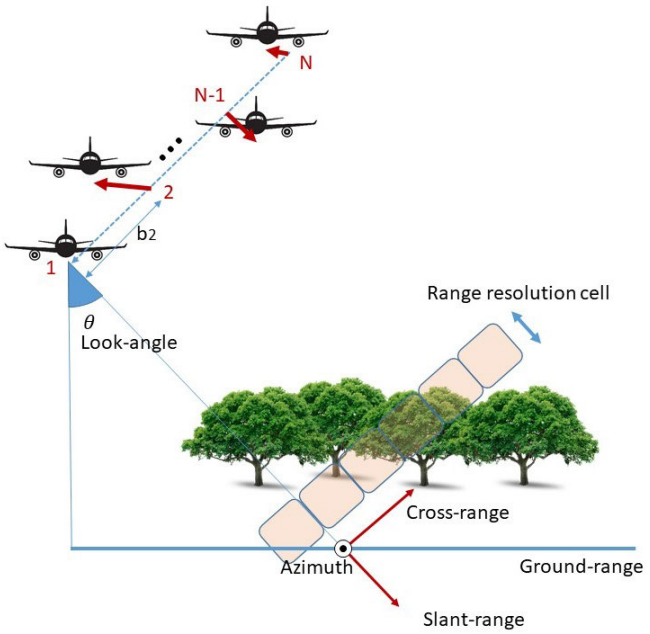

Fig. 1. Airborne multibaseline tomographic SAR imaging system: geometrical scheme. The azimuth axis is perpendicular to the sheet.

strategies. The SLC images are assumed coregistrated with respect to a reference (primary) image and, for the airborne case, motion compensated. It is also assumed that they are compensated for the range-dependent phase component (terrain topography compensation) at the data preprocessing stage. The latter operation relies on the knowledge of an external digital elevation model (DEM), but more important on the accurate knowledge of the sensors' positions at subwavelength scale. DEM errors translate to a simple vertical shift of the tomographic profile. Conversely, the inaccurate knowledge of the sensors' positions leads to disturbing phase terms (phase artifacts) related to the inherent variation of the sensor–target distance with respect to the nominal one. Such space-variant phase artifacts, if not estimated and compensated, hamper the well-focused 3-D tomographic reconstruction.

More formally, the MB complex-valued SAR data stack corrupted by such phase artifacts can be described according to the following discrete model (see Fig. 1) [25]:

$$\boldsymbol{u} = \boldsymbol{a} \odot \mathbf{H}(\boldsymbol{s})\boldsymbol{\gamma}(\boldsymbol{s}) + \boldsymbol{w} \tag{1}$$

where $\boldsymbol{u} = [u_{xr}^1, \ldots, u_{xr}^N]^{\mathrm{T}} \in \mathbb{C}^N$ is the SAR observable data stack, u_{xr}^i refers to the ith SLC image pixel, and x and r being the subscripts denoting the azimuth and range (discrete) pixel coordinates, respectively. The superscript T denotes the transposition operation and $\odot$ is the Hadamard product. Moreover, the following notation has been adopted:

1) $\boldsymbol{\gamma}(\boldsymbol{s}) = [\gamma_{xr}(s_1), \ldots, \gamma_{xr}(s_K)]^{\mathrm{T}} \in \mathbb{C}^K$ is the complex vector describing a sampled version of the (unknown) complex reflectivity distribution along the cross-radial direction at a prescribed range–azimuth location;
2) $\boldsymbol{s} = [s_1, \ldots, s_K]$ is the vector collecting the (discrete) cross-radial positions $s_k, k = 1 \ldots, K$;

3) K is the relevant number of samples corresponding to the discretization of the unknown distribution;
4) $\mathbf{H}(\boldsymbol{s}) = [\boldsymbol{h}(s_1), \ldots, \boldsymbol{h}(s_K)]$ is the $N \times K$ sensing matrix;
5) $\mathbf{h}(s_k) = [\exp(-j2\pi\xi_1 s_k), \ldots, \exp(-j2\pi\xi_N s_k)]^{\mathrm{T}}$ is commonly referred to as the steering vector, thus representing the column vectors of $\mathbf{H}(\boldsymbol{s})$ containing the interferometric phase information associated with a scatter located at cross-range position s_k;
6) $\xi_n = 2b_n/(\lambda r)$ is the (two-way) spatial frequency associated to the nth and primary tracks;
7) b_n is the perpendicular baseline (antenna position) of the nth track relative to the primary track along the s-axis;
8) λ is the operative radar wavelength;
9) $\boldsymbol{w} \in \mathbb{C}^N$ is an additive noise term.

and finally, the vector

$$\boldsymbol{a} = \left[e^{j\chi_{xr}^1}, \ldots, e^{j\chi_{xr}^N}\right]^{\mathrm{T}} \tag{2}$$

collects the unknown phase disturbing components.

According to the adopted model, the complex-valued information associated with a pixel of the nth SLC image, d_{xr}^n, results from the coherent superposition of the contributions from the scatters at different cross-radial (or elevation) locations pertaining to that pixel

$$u_{xr}^n = e^{j\chi_{xr}^n} \sum_{k=1}^{K} \gamma_{xr}(s_k) e^{-j2\pi\xi_n s_k} \tag{3}$$

where $\gamma_{xr} : s_k \in \mathbb{R} \to \mathbb{C}$ is the target scattering distribution along the elevation direction.

Equation (3) shows that, except for the disturbing phase term $e^{j\chi_{xr}^n}$, the RHS describes an irregularly sampled discrete Fourier transform of the scene (complex) reflectivity distribution along the cross-radial direction. We stress that, in the limit of the approximations made, (3) essentially states that the MB SAR data and the scene complex reflectivity distribution within each resolution cell constitute a Fourier pair [1], [5].

The TomoSAR problem to be addressed involves the recovery of the target scattering function $\gamma_{xr}(s_k)$, utilizing the complex observations u_{xr}^n with $n \in (1, \ldots, N)$. It should then be clear that each nth space-variant phase distribution χ_{xr}^n (PHS) has to be preliminarily estimated and compensated before proceeding with the proper tomographic reconstruction of the 3-D radar reflectivity.

A key parameter in TomoSAR imaging is the vertical resolution Δz, which can be approximately written as follows (Rayleigh limit) [1], [5]:

$$\Delta z \simeq \frac{2\pi}{\max_n\{k_z^n\} - \min_n\{k_z^n\}} \tag{4}$$

wherein k_z^n is the vertical (interferometric) wavenumber referred to the primary image. According to the literature [1], [5], k_z^n can be related to the nominal (orthogonal component) baseline b_n by means of the following:

$$k_z^n = \frac{2\pi\xi_n}{\sin\theta} = \frac{4\pi b_n}{\lambda r \sin\theta} = \frac{2\pi}{H_{2\pi}^n}. \tag{5}$$

In (5), θ is the radar look angle, $H_{2\pi}^n$ is the height of ambiguity of the nth acquisition, and $z = s\sin\theta$ being the vertical coordinate, where s is the (continuous) cross-radial coordinate. Note that, due to the topographic relief viewed by SAR side-looking imaging system, θ is generally dependent on both the azimuth and range coordinates, i.e., $\theta = \theta_{xr}$. According to (5), such a dependence is also inherited by k_z^n in addition to the intrinsic dependence associated with ξ_n (due to the line-of-sight dependence on the azimuth and range of the orthogonal baseline b_n). For the sake of notation simplicity, spatial dependence on x and r of b_n and k_z^n (and consequently of $H_{2\pi}^n$) has been understood.

A remark is now in order. The phase calibration problem concerns the estimation (for any pixel) of the unknown vector $\boldsymbol{a}$ in (2). Anyway, as a consequence of the fact that a constant (n-independent) phase factor, variable with x and r, does not affect the vertical focusing operation, phase calibration is required for $N-1$ acquisitions. In other words, the unknowns of our problems are $N-1$ phase differences evaluated from the N phase components of (2) evaluated with respect to a reference acquisition, typically the selected primary acquisition. The estimation of the unknown phase values can be conveniently addressed in the interferometric framework, where generally different strategies for generating the observable (known) interferometric phase values are commonly adopted. One possibility, referred to as Single-Master (SM) interferometric pairing, involves the evaluations of the observable interferometric phases with respect to the unique primary image. In this case, the observable reflects the same structure of the unknowns and measurement redundancy is not exploited in the interferometric processing. The processing involves the generation of large baseline interferograms which are typically more critical in terms of decorrelation phenomena. An alternative strategy to circumvent the problem is to refer to a Multi-Master (MM) strategy [28], [29], in which only small baseline interferograms are used. The unique reference primary image involved in the data preprocessing stage is sometimes referred to as super-primary, and typically, redundancy is exploited according to different network topologies, as discussed in Section II-B. To avoid the large baseline interferograms, M is typically lower than the number of all possible pairings, i.e., $N(N-1)/2$, for instance between N and $3N$.

It is worth finally noting that (5), defined for the SM interferometric pairing, can be considered valid, *mutatis mutandis*, also for the MM case.

B. Interferometric Network Formulation

In the formulation of the problem at hand, involving the process of pairing acquisitions, a graph-based description naturally arises for both the SM and MM cases. In the rigorous methodological framework of the *discrete calculus*, the topological properties of a graph can be captured by differential operators that are phrased as algebraic structures. We refer to [30], [31], and [32] for graph–theoretic notions and discrete calculus application to SAR interferometry, respectively. Some basic aspects are briefly recalled in the following.

A graph $\mathcal{G} = (\mathcal{V}; \mathcal{E})$ can be formally defined by two sets, being $\mathcal{V}$ the set of vertices with cardinality N and $\mathcal{E}$ the set of

edges with cardinality M. For our purposes, we specifically refer to acyclic directed graphs [30], [31]. Furthermore, the vector space $\mathbb{R}^M$ is referred to as the edge space (e.g., representing the interferometric observation) and the vector space $\mathbb{R}^N$ is referred to as the vertex space (e.g., representing the SLC acquisitions), with $\mathbb{R}$ denoting the field of real numbers. In particular, the $M \times N$ *incidence matrix* $\mathbf{\Pi} = [\Pi_{mn}]$ of an oriented graph $\mathcal{G}$ specifies its edge–node connectivity relations. Its entries are defined as follows [32]:

$$\Pi_{mn} = \begin{cases} -1, & \text{for if } m\text{th edge starts at } n\text{th node} \\ +1, & \text{for if } m\text{th edge ends at } n\text{th node} \\ 0, & \text{for otherwise} \end{cases} \tag{6}$$

with $m = 1, \ldots, M$ and $n = 1, \ldots, N$. Note that, for a connected graph, the column rank of $\mathbf{\Pi}$ is $N - 1$. Therefore, the right null space of the edge–node incidence matrix $\mathbf{\Pi}$ is spanned by the set of constant-valued vectors ($\mathbf{\Pi} \boldsymbol{c} = 0$ with $\boldsymbol{c} = [c, \ldots, c] \in \mathbb{R}^N$).

Note that a graph is connected when there exists a path (i.e., a set of edges) between every pair of vertices. The minimum number of edges required to build a connected graph is evidently $M = N - 1$. Typically, the interferogram generation involves a (redundant) network ($M > N - 1$) defined according to a small-baseline strategy [28].

The incidence matrix $\mathbf{\Pi}$ generates an orthogonal decomposition $\mathcal{R}(\mathbf{\Pi}) \bigoplus \mathcal{N}(\mathbf{\Pi}^{\mathrm{T}}) = \mathbb{R}^M$, where $\mathcal{R}(\mathbf{\Pi})$ is the column space of $\mathbf{\Pi}$, $\mathcal{N}(\mathbf{\Pi}^{\mathrm{T}})$ denotes the *kernel* (or null space) of the matrix $\mathbf{\Pi}^{\mathrm{T}}$, and $\bigoplus$ denotes the direct sum operator. The operator $\mathbf{\Omega}$, referred to as the cycle matrix, can also be defined [32]. Remarkably, the topological operators $\mathbf{\Pi}$, $\mathbf{\Pi}^{\mathrm{T}}$, and $\mathbf{\Omega}$ provide the discrete counterparts of the classical *gradient* (∇), *divergence* ($\nabla\cdot$), and *curl* ($\nabla\times$) operators of the vector calculus for continuous space, respectively [32].

In particular, the vertex-to-edge problem to be inverted is discussed. Given an arbitrary $\mathbf{f} \in \mathbb{R}^M$, we consider the following equation:

$$\mathbf{\Pi}\, \mathbf{d} = \mathbf{f} \tag{7}$$

where $\mathbf{\Pi}$ is the discrete gradient defined in (6) and $\mathbf{d} \in \mathbb{R}^N$. The solution of (7) (if it exists) is called the potential of $\mathbf{f}$.

From (7), we get

$$\mathbf{\Pi}^{\mathrm{T}} \mathbf{\Pi}\, \mathbf{d} = \mathbf{\Pi}^{\mathrm{T}} \mathbf{f} \tag{8}$$

where $\boldsymbol{L} = \mathbf{\Pi}^{\mathrm{T}} \mathbf{\Pi}$ is the (discrete) *Laplacian* operator. The symmetric and positive semidefinite matrix $\boldsymbol{L}$ does not depend on the orientation of $\mathcal{G}$, it describes the connectivity of the graph structure and represents the discrete counterpart of the Laplacian in continuous domain (∇^2). When the graph is connected, the null- pace of $\boldsymbol{L}$ is the 1-D space spanned by a constant vector. Hence, $\boldsymbol{L}$ has at least one zero eigenvalue and it is therefore rank-deficient. More specifically, the multiplicity of the zero eigenvalue of the Laplacian matrix corresponds to the number of connected components in the graph [33]. For a connected graph (as assumed hereinafter), the rank of the $\boldsymbol{L}$ matrix is $N - 1$, i.e., equal to the number of unknowns of PHS estimation problem.

The reduced incidence matrix, $\mathbf{\Pi}_0$, formed by removing the column corresponding to the reference node (i.e., a reference acquisition for the MB case at hand), has a right null space of dimension zero [30]. Subsequently, the reduced Laplacian matrix $\boldsymbol{L}_0 = \mathbf{\Pi}_0^{\mathrm{T}} \mathbf{\Pi}_0$ has full rank. Therefore, from (8), we obtain

$$\mathbf{d} = \mathbf{\Pi}_0^{\dagger} \mathbf{f} \tag{9}$$

where $\mathbf{\Pi}_0^{\dagger}$ is called the *Moore–Penrose* inverse (left pseudo inverse) of $\mathbf{\Pi}_0$. It is given in the form

$$\mathbf{\Pi}_0^{\dagger} = \left(\mathbf{\Pi}_0^{\mathrm{T}} \mathbf{\Pi}_0\right)^{-1} \mathbf{\Pi}_0^{\mathrm{T}}. \tag{10}$$

A weighted inversion can be also considered

$$\mathbf{d} = \mathbf{\Pi}_{0,\mathbf{W}}^{\dagger} \mathbf{f} \tag{11}$$

where $\mathbf{W}$ is the M-dimensional diagonal matrix of edge weights, and the matrix $\mathbf{\Pi}_{0,\mathbf{W}}^{\dagger}$ is the weighted left pseudo inverse of $\mathbf{\Pi}_0$ expressed as follows:

$$\mathbf{\Pi}_{0,\mathbf{W}}^{\dagger} = \left(\mathbf{\Pi}_0^{\mathrm{T}} \mathbf{W} \mathbf{\Pi}_0\right)^{-1} \mathbf{\Pi}_0^{\mathrm{T}} \mathbf{W}. \tag{12}$$

The inversion procedure involving the incidence matrix can also be obtained through singular value decomposition (SVD). This approach is analogous to the commonly employed method in Small Baseline Subset (SBAS) processing [28].

C. Space-Varying Phase Screen Model

The adopted PHS model is briefly described in this section. The geometry of the airborne MB SAR imaging system is shown in Fig. 1. Since the atmospheric perturbations are limited for airborne systems, we only take into account inaccuracies in the antennas' positions. Available IMUs are generally able to measure trajectory deviations up to a few centimeters, which is not adequate even at P-band. For a fixed azimuth position, the phase contribution α pertaining to the generic ith sensor trajectory uncertainty is given in the form [8]

$$\alpha\left(\delta \boldsymbol{S}_x^n, \theta_{xr}\right) = -\frac{4\pi}{\lambda} \delta \boldsymbol{S}_x^n \cdot \hat{\mathbf{r}}(\theta_{xr}) \tag{13}$$

where θ_{xr} is the previously defined look angle (or off-nadir angle), $\hat{\mathbf{r}}(\theta_{xr}) = [-\sin\theta_{xr}, \cos\theta_{xr}]^{\mathrm{T}}$ is the radial unit vector, and $\delta \boldsymbol{S}_x^n = [\delta S_y^n, \delta S_z^n]^{\mathrm{T}}$ is the azimuth-variant position error vector of the nth platform, with δS_y^n and δS_z^n denoting its ground range and height (i.e., horizontal and vertical) components, respectively. It should be noted that unavoidable unknown constant (i.e., invariant with respect to azimuth and range) phase offsets have been understood and suppressed in (13), as they do not affect the subsequent model-based optimization. These phase offsets, typically present in tomographic analysis, must be estimated and compensated after the estimation of residual trajectory deviations.

It should be noted that, for any generic acquisition pair (p, q), we get

$$\alpha\left(\delta \boldsymbol{S}_x^q, \theta_{xr}\right) - \alpha\left(\delta \boldsymbol{S}_x^p, \theta_{xr}\right) = \alpha\left(\delta \boldsymbol{S}_x^{pq}, \theta_{xr}\right). \tag{14}$$

According to (14), the PHS affecting the interferometric phase depends on the relative position error $\delta \boldsymbol{S}_x^{pq} = \delta \boldsymbol{S}_x^q - \delta \boldsymbol{S}_x^p$. Noted that (6) uniquely defines the mapping $e_m = (p, q) \in \mathcal{E} = \{e_1, \ldots, e_M\} \rightarrow p, q \in \mathcal{V} = \{1, \ldots, N\}$, with $p \neq q$.

Therefore, for each $n \in \{1, \ldots, N\}$, the (unknown) space-variant phase screen $\chi_{xr}^n = \alpha(\delta \boldsymbol{S}_x^n, \theta_{xr})$ uniquely impairing the nth SAR acquisition has to be estimated and properly compensated for, as discussed in the following.

III. Phase-Screen Estimation and Compensation

Regardless of the adopted interferometric pairing strategy, i.e., SM or MM, the problem of estimating the unknown PHSs can be addressed by either considering a disjoint or a joint strategy, as discussed in the following. Obviously, if the SM strategy is adopted, both the disjoint and joint estimation directly provides the $N-1$ phase unknowns required for the phase calibration. Conversely, as discussed in Section II-B, for the MM disjoint estimation case a further inversion procedure is required to convert the (M) estimated phase errors to the corresponding $N-1$ phase unknowns required for the calibration of the data stack $\boldsymbol{u}$ in (1).

A. Disjoint Phase-Screen Estimation

An estimation of the position errors $\delta \hat{\boldsymbol{S}}_x^{pq}$ can be achieved, for each $e_m = (p, q)$ (edge) of the M interferometric pairs of the (graph) network, according to the following optimization problem:

$$\delta \hat{\boldsymbol{S}}_x^{pq} = \operatorname{argmin}_{\delta \boldsymbol{S}_x^{pq}} \left(1 - \left|F\left(\delta \boldsymbol{S}_x^{pq}\right)\right|\right) \tag{15}$$

where the function $F(\delta \boldsymbol{S}_x^{pq})$ is given in the form [8]

$$F\left(\delta \boldsymbol{S}_x^{pq}\right) = \frac{1}{R} \sum_{r=1}^{R} c_{xr} e^{j\left(\hat{\phi}_{xr}^{pq} - \alpha\left(\delta \boldsymbol{S}_x^{pq}, \theta_{xr}\right)\right)} \tag{16}$$

wherein the function α is defined in (13), R is the number of range pixels, $\hat{\phi}_{xr}^{pq}$ denotes the observed interferometric phase, and c_{xr} is a suitable weighting function. As usual, the subscripts x and r indicate the azimuth and range (discrete) coordinates of the pixel, respectively. Note that the objective function involved in (15) is insensitive to a constant phase, thus overcoming the local minimum problem in the optimization, as highlighted in [8]. As a result, x-dependent (r-independent) phase offsets must be estimated after the optimization for each interferometric pair. The final estimated phase screen is thus the combination of the estimated xr-dependent phase function described by the model in (13), depending on the estimated residual navigation errors, and the x-dependent component subsequently estimated to account for the phase offsets, including the constant one suppressed in (13).

According to (15)–(16), the phase-screen estimation problem has been broken down into a series of M subproblems, each for a different interferometric pair (i.e., a graph edge) $e_m = (p, q) \in \mathcal{E}$, to be solved independently. For an arbitrary configuration (SM or MM), according to (11), we obtain

$$\left[\delta \mathbf{y}_x, \delta \mathbf{z}_x\right] = \boldsymbol{\Pi}_{0,\mathbf{W}}^{\dagger} \left[\delta \mathbf{u}_x, \delta \mathbf{v}_x\right] \tag{17}$$

where $\boldsymbol{\Pi}_{0,\mathbf{W}}^{\dagger}$ is given by (12), and the azimuth-variant vectors $\delta \mathbf{y}_x = [\delta S_y^n] \in \mathbb{R}^N$ and $\delta \mathbf{z}_x = [\delta S_z^n] \in \mathbb{R}^N$ collect the horizontal and vertical components of platform position-error vectors, respectively. Similarly, the azimuth-variant vectors $\delta \mathbf{u}_x = [\delta S_y^m] \in \mathbb{R}^M$ and $\delta \mathbf{v}_x = [\delta S_z^m] \in \mathbb{R}^M$ collect the horizontal and vertical components of position-error vectors associated with the inherent interferometric pairs (edges), respectively. Moreover, the weights in $\mathbf{W}$ are defined according to suitable indexes accounting for the variability in the quality of the interferograms (e.g., average coherence of the interferograms).

Some further remarks concerning the limitations inherent to the description provided by the function $\left|F(\delta \boldsymbol{S}_x^{pq})\right|$ are now in order [see (15)–(16)].

First, the model in (13) assumes that the effective phase center height is perfectly known, via θ_{xr}. However, in the presence of a (space-variant) residual height, the phase can be affected by a residual component, which may impair the estimation of the unknown deviation $\delta \boldsymbol{S}_x^{pq}$ in (15). To cope with this problem, the double-localization method was proposed in [8]. The residual height of the scatterers can be in this case estimated pixel-by-pixel by using an approach similar to the one used in the well-known PS method, involving the canonical periodogram computed from the available (uncompensated) multibaseline stack, see [8], [34]. The estimated residual heights can then be used to update θ_{xr} in (13), and subsequently solve (15) to compute (separately) the unknown trajectory deviations. The procedure can be iterated up to a suitable convergence.

Second, the model in (13) implicitly assumes that the scattering is concentrated at a certain height. In the presence of a distributed vertical scattering, such as the forest, θ_{xr} can be no longer associated distinctively with the scatterer. A possible approach to deal with this problem is to resort to an equivalent (pointlike) scatterer concentrated at a certain altitude through the so-called "phase linking," which can be achieved through "SqueeSAR" [35] or principal component analysis (CAESAR) methods [36]. The location of the equivalent (pointlike) scatterer is commonly referred to as the *phase center* of the extended target. Both methods, double localization and phase linking, were, however, not implemented in this work for the reasons explained in Section V.

B. Joint Phase-Screen Estimation

In order to perform a robust estimation of the trajectory deviations, we consider the following joint estimation problem. The idea involves defining a suitable joint cost function, taking into account each interferometric pair (p, q) of the redundant network (i.e., $\mathcal{G}$) specified in the construction of the interferometric stack. This cost function encompasses all relative deviations in position compared to that of the primary, $\delta \boldsymbol{S}_x^n$ with $n \in (1, \ldots, N-1)$, aiming at minimizing them conjointly. Accordingly, in a general form, the estimation problem can be stated mathematically in terms of the following optimization problem:

$$\begin{aligned} &\delta \hat{\boldsymbol{S}}_x^1, \delta \hat{\boldsymbol{S}}_x^2, \ldots, \delta \hat{\boldsymbol{S}}_x^{N-1} \\ &\quad = \underset{\delta \boldsymbol{S}_x^1, \delta \boldsymbol{S}_x^2, \ldots, \delta \boldsymbol{S}_x^{N-1}}{\operatorname{argmin}} \left(1 - J\left(\delta \boldsymbol{S}_x^1, \delta \boldsymbol{S}_x^2, \ldots, \delta \boldsymbol{S}_x^{N-1}\right)\right) \end{aligned} \tag{18}$$

where J is a suitable cost function.

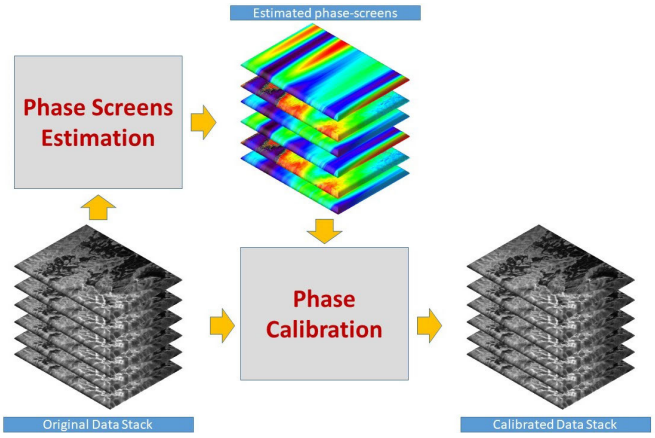

Fig. 2. Phase compensation workflow based on phase-screen (joint) estimation method.

For our scopes, we specify J in the form

$$J\left(\delta \boldsymbol{S}_x^1, \delta \boldsymbol{S}_x^2, \ldots, \delta \boldsymbol{S}_x^{N-1}\right) = \sum_{(p,q)\in\mathcal{E}} \left|F\left(\delta \boldsymbol{S}_x^{pq}\right)\right| \tag{19}$$

where $\mathcal{E} = \{e_1, \ldots, e_M\}$ is the set of the graph edges $e_m = (p, q)$ (associated with the selected interferometric pairs), and F is defined in (16). It should be emphasized that the objective function in (18) has been purposely defined to be, similar to the one pertinent to the disjoint approach, insensitive to constant phase offsets, thus mitigating the mentioned local minimum problem in the associated optimization. The solution of the inherent *nonlinear* optimization problem can be obtained through suitable numerical methods.

Note that, according to the above specification, the optimization process involves all the suitably selected (M) interferograms, which generally represents a subset of all $(N(N-1)/2)$ the possible interferograms.

C. Phase Calibration and Tomography Processing

After obtaining model parameters through joint estimation (18)–(19) or disjoint estimation (15)–(16) and (17), the reconstructed PHS affecting the nth acquisition is obtained as follows:

$$\chi_{xr}^n = \alpha\left(\delta \hat{\boldsymbol{S}}_x^n, \theta_{xr}\right) \tag{20}$$

where $\delta \hat{\boldsymbol{S}}_x^n$ represents the estimation of the position deviation of the nth acquisition with respect to the primary track. Therefore, all the phase screens χ_{xr}^n with $n \in (1, \ldots, N-1)$ can be retrieved and suitably compensated (also see Fig. 2). We highlight that, for each range line, x-dependent phase offsets are estimated by means of a weighted average in the complex domain. Accordingly, the final estimated phase screen is thus, for both the disjoint and joint methods, the composition of the estimated xr-dependent phase function described by the model in (13) related to the residual navigation errors, and the x-dependent phase offsets. Coherence information is also suitably incorporated into the weighting strategy.

Once the PHS estimation has been achieved according to the method presented in Section II, a proper phase calibration (Fig. 2) is then performed by removing the retrieved phase screens from the multibaseline SLC data stack, see (3). Subsequently, the distribution of the scene complex reflectivity along cross-range direction at each range–azimuth location (xr) can be properly reconstructed via 3-D coherent focusing (multibaseline SAR tomography), as further discussed in the following [22].

The general inversion problem underlying TomoSAR estimation of $\boldsymbol{\gamma}$ can be addressed by adopting spectral estimation methodologies [37]. Among the commonly used spectral estimators, the conventional beamforming (BF) method is widely used and specifically applied here. For a given set of steering vectors, the power of spatial spectrum estimated by BF is given in the form

$$\left|\hat{\gamma}_{BF}(s_k)\right|^2 = \frac{\mathbf{h}^\dagger(s_k)\hat{R}_{\mathbf{dd}}\mathbf{h}(s_k)}{N^2} \tag{21}$$

where N is the number of tracks, s_k with $k \in (1, \ldots, K)$ is the cross-radial coordinate, $\hat{\gamma}$ denotes the estimated reflectivity distribution along the cross-radial direction, $\mathbf{h}(s_k)$ is the steering vector defined in Section II-A, $\mathbf{R}_{\mathbf{dd}} = \langle \mathbf{d}\mathbf{d}^\dagger \rangle$ is the complex covariance matrix of the multibaseline SAR data, $\hat{R}_{\mathbf{dd}}$ denotes the maximum-likelihood estimation of $\mathbf{R}_{\mathbf{dd}}$, the crochets represent statistical average, and the superscript † is the Hermitian conjugate operator. Notice that $\hat{R}_{\mathbf{dd}}$ can be obtained, for a fixed pixel, over L looks using an estimation window centered on that pixel [38]

$$\hat{\mathbf{R}}_{\mathbf{dd}} = \sum \mathbf{d}\mathbf{d}^\dagger. \tag{22}$$

Alternatively, tomographic inversion can be achieved by using the Capon filter [38]. Although it permits typically better performance in terms of cross-range resolution and sidelobe suppression compared to Fourier BF (with which the Rayleigh resolution is approximately achieved), Capon optimization introduces biases in the radiometric reconstruction of the (forest) volume scattering contributions [39].

In this work, we have used the classical BF in order to better highlight the differences in the reconstructions achieved by the different phase compensation methods.

IV. Experimental Results

This section presents the results obtained by processing real-airborne multibaseline SAR data with the aim of evaluating the effectiveness of the proposed joint phase calibration and compare it to the classical, disjoint method.

A. Study Area

In the framework of the AfriSAR campaign, four different test sites (Lopé, Mondah, Rabi, and Mabounie) were chosen for a fully polarimetric multibaseline SAR data acquisition carried out by the Office National d'Etudes et de Recherches Aérospatiales (ONERA) (July 2015) and the German Aerospace Center (DLR) (February 2016) [27].

In particular, the inherent acquisitions over Lopé site are specifically oriented to tomographic analyses and, therefore, this site is selected for our investigation. Lopé site is located near the geographical center of Gabon (north-east Africa) within Lopé National Park, which is part of the World Heritage

TABLE I
AIRBORNE SAR SYSTEM PARAMETERS

Parameter	Quantity
Look Direction	left
Near Range	6600 m
Wavelength	0.689 m
Carrier Frequency	435.0 MHz
Pulse duration	30 μs
Bandwidth	50.0 MHz
Effective Pulse Repetion Frequency (PRF)	1250.0 Hz
Flight ground altitude	6096.0 m
Range of look angle	21-51 deg
Elevation Resolution	12.5 m
Azimuth Spacing	1.20 m
Range Spacing	2.40 m
Azimuth resolution	2.00 m
Range Resolution	3.90 m
Azimuth Lines	8642
Range samples	1300

List of UNESCO. Lopé National Park is one of the largest national parks in central Gabon, covering an area of roughly 5000 km^2; thus, Lopé area is mainly characterized by predominantly hilly inland tropical forests. Despite the prevalent rainforest terrain with trees ranging from 30 to 40 m, the northern part of the scene is composed of the last remnants of a grass savanna characterized by low vegetation [40].

As a result, the Lopé site constitutes an interesting study area featuring substantial topography, with a DEM altitude ranging from 0 to 600 m. Additionally, it shows structural diversity, characterized by a mosaic of savannah and dense primary forest, and a wide range of biomass, varying from 60 to 600 tons per hectare.

B. Airborne SAR Dataset

The SAR data stack used for the experiments carried out in this article are obtained in the framework of the AfriSAR campaign (July 2015) conducted in Gabon, West Africa. This data was provided by the European Space Agency (ESA) under science proposal (Project 69872).

We use AfriSAR data acquired by the SETHI airborne SAR system developed by ONERA and onboard a Falcon 20 aircraft. Specifically, we focus on the data collection acquired by ONERA at P-band over the tropical forests in the Lopé region (National Park in Gabon). The dataset collected over the Lopé study area had baseline distribution specifically designed for TomoSAR investigations. Furthermore, this dataset is interesting due to the under-foliage penetration capabilities of P-band wavelengths. The tomographic P-band dataset consists of 12 fully polarimetric SLC data.

The main system parameters are listed in Table I. Further details about the AfriSAR campaign can be found in [40]. Acquisition with acquisition number $n = 6$ is considered the super-primary image. Moreover, the values of the parameter k_z^n, defined in (5), are referred to the super-primary acquisition and are represented as a function of the acquisition number n in Fig. 3.

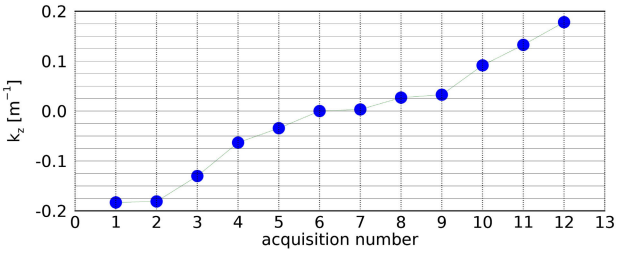

Fig. 3. $k_z^n[m^{-1}]$ referred to the (super-primary) acquisition ($n = 6$) is represented as a function of the acquisition number n.

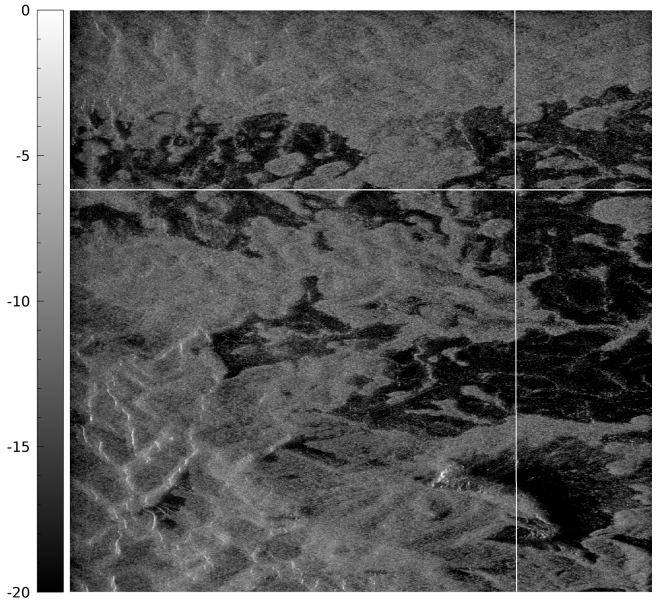

Fig. 4. σ^0 (dB) obtained via multitemporal averaging. The azimuth direction is from bottom to top, the range direction is from left to right. The white lines indicate the positions of the tomographic cuts presented in Section IV-D.

Moreover, the SAR dataset is given in terms of the backscattering coefficient σ^0 [41], [42], [43]. In particular, in Fig. 4, the backscattering coefficient σ^0 (dB) obtained via multitemporal averaging is depicted in the range $(-20, 0$ dB). The azimuth direction is from bottom to top, and the range direction is from left to right.

C. Airborne LiDAR Dataset

Land Vegetation and Ice Sensor (LVIS) is a medium-altitude imaging laser altimeter designed and developed at the NASA [40]. LVIS data products include Level 1B (geolocated waveforms) and 2B (elevation and height products). We used the Level 2 product containing elevation (ground and canopy top) and relative height (RH), which were derived from the Level 1B products containing the geolocated laser return waveforms in HDF5 format. Specifically, to validate the TomoSAR results, we used products provided at a 25 m resolution data acquired by the LVIS instrument for the selected Lopé forested site, collected during the 2016 NASA-ESA AfriSAR campaign [44].

The height metrics RH25, RH50, RH75, RH90, RH95, RH98, RH99, and RH100 were computed from the LiDAR waveform, where RHX is defined as the height relative to the

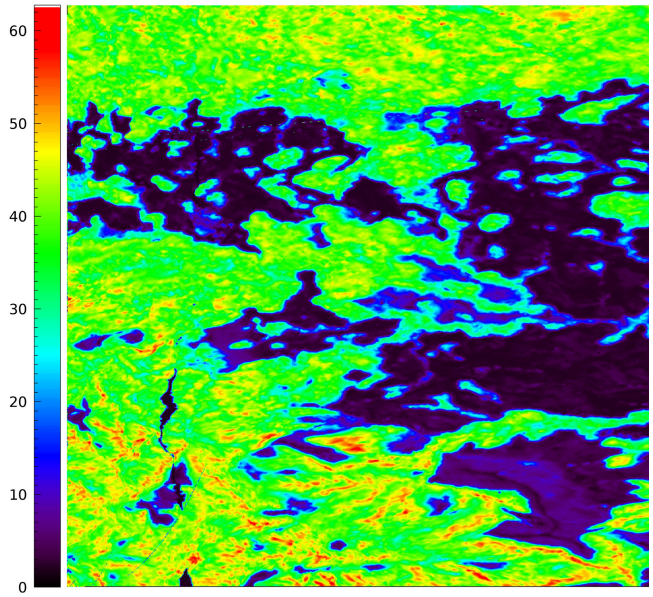

Fig. 5. LiDAR RH99 metric (in meters).

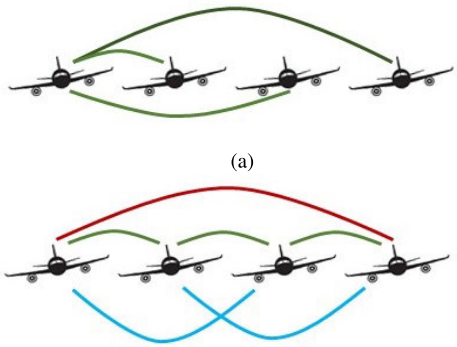

(a)

(b)

Fig. 6. Two exemplary network configurations. (a) SM configuration. (b) MM configuration including distances of 1 (green), 2 (blu), and 3 (red).

ground (denoted as "RH") at which there is the percentile X% of the accumulated total waveform energy from the last detectable return. For example, RH50 represents the height below which there is 50% of the LiDAR return energy. RH98, RH99, and RH100 can be used to represent the top canopy height. The LVIS 25 $\times$ 25 m (0.0625 ha) spatial resolution relative height metrics and bare Earth elevation grids were generated from the footprint elevation and height metrics [45]. All LVIS gridded products are provided in the GeoTIFF format. In particular, the representation of the metric R99 in the SAR image domain is provided in Fig. 5.

D. PHS Estimation and TomoSAR Results

In this section, we present the results achieved by the classical (disjoint) and proposed (joint) phase calibration methods, obtained by using different network configurations. Note that both SM and MM observations can be described by suitably specifying the sequence of all the edges in $\mathcal{E}$.

In Fig. 6, by way of example for the simplified case of 4 acquisitions, the SM configuration and the used MM configurations, including pairing with distances of 1, 2, and 3, are schematically depicted. Acquisitions are supposed to be ordered according to the spatial baseline; pairing with distance 1 is hereafter also referred to as sequential pairing.

Numerical optimization was carried out by using the well-known, efficient, and derivative-free Powell optimization method. First, the PHSs reconstructed by using the different estimation approaches and configurations are illustrated by focusing on selected interferometric pairs (Figs. 7–9).

In Fig. 7, the obtained results specifically refer to the acquisitions 5 and 6 of the multibaseline SAR data stack. By direct inspection of Fig. 7(a), the effect of the airborne instability on the interferometric phase (observable) can be directly recognized. In particular, it becomes evident that a slow, oscillating (disturbing) residual phase is presented [see Fig. 7(a)]. The reconstructed PHSs achieved with the classical (disjoint) estimation approach, for SM configuration [corresponding to the network topology depicted in Fig. 6a)] and for the MM configuration including sequential pairing, i.e., pairing with distance 1 [corresponding to the network topology depicted in green in Fig. 6b)], are depicted in Fig. 7(b) and (c), respectively. Finally, Fig. 7(d) shows the PHS obtained with the proposed (joint) estimation method for the MM configuration including pairs with distances 1, 2, and 3, whose topology is schematically represented in Fig. 6(b).

By comparing the patterns in Fig. 7, it is then clear that the proposed approach demonstrates a significant capability in reconstructing the PHS, thereby estimating a more regular pattern. As shown later, this enables a more accurate phase calibration of the data stack, leading to higher quality reconstructed tomographic profiles.

A remark is now in order. It should be noted that the PHSs shown in Fig. 7(b) and (c), achieved via the disjoint estimation algorithm, are obtained directly from the interferogram shown in Fig. 7(a). This is a consequence of the fact that the acquisition pair 5 and 6 (super-primary) belongs to both the set of edges defined by the topologies associated with the SM and MM with distance 1 configurations.

Furthermore, Fig. 8 shows the compensated interferometric phase for the acquisition pair 5 and 6, obtained using (a) disjoint PHS estimation and SM configuration, and (b) the joint PHS estimation and MM configuration. As can be seen from Fig. 8, the joint estimation approach enables a more robust phase screen reconstruction with a residual phase closer to zero.

A different case, involving the acquisition pair 6 (super-primary) and 8, is analyzed in Fig. 9. Note that in this case the selected interferometric pair belongs to a set of edges defined by the topologies associated with the SM configuration, but not to the one associated with MM configuration with sequential pairing. As a consequence, in the disjoint estimation processes, while the PHS shown in Fig. 9(b) is directly estimated from the interferogram shown in Fig. 9, the PHS shown in Fig. 9(c) is achieved by combining the PHS between acquisitions 6 and 7 and the PHS between acquisitions 7 and 8.

Similar to the previous case represented in Fig. 7, the PHS estimated by the joint approach shown in Fig. 9(d)

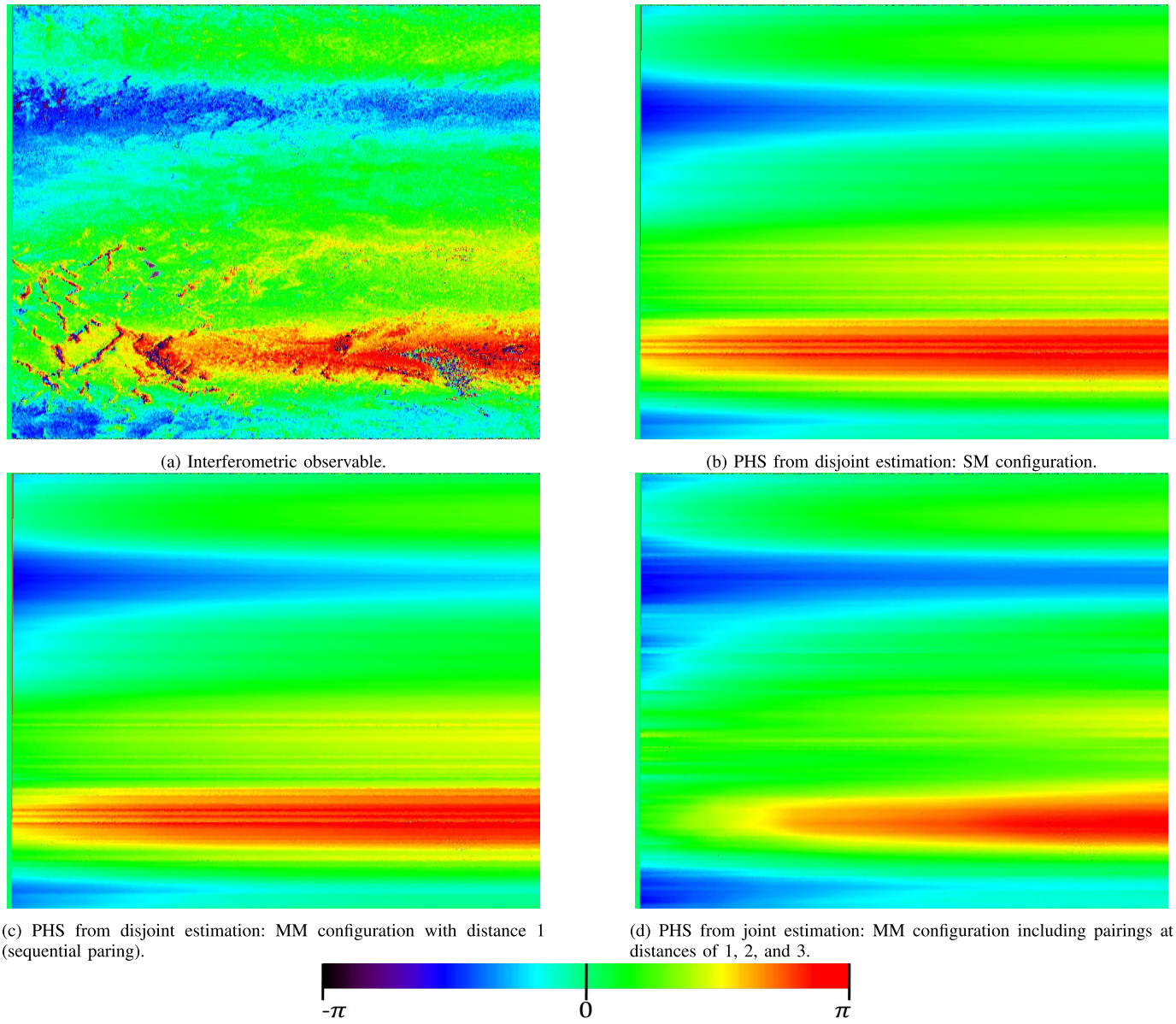

(a) Interferometric observable.

(b) PHS from disjoint estimation: SM configuration.

(c) PHS from disjoint estimation: MM configuration with distance 1 (sequential paring).

(d) PHS from joint estimation: MM configuration including pairings at distances of 1, 2, and 3.

Fig. 7. Results obtained for the pair of acquisitions 5 and 6. (a) Interferometric phase (observable), and the corresponding phase screens (PHSs) reconstructed with the classical (disjoint) estimation approach, for (b) SM and (c) MM configurations, and with (d) proposed (joint) estimation approach for the MM configuration.

exhibits a more regular pattern with respect to the other cases corresponding to disjoint estimation.

The analysis of the performance of the different estimation strategies is now assessed in terms of tomographic reconstruction capabilities. In particular, Fig. 10 shows the P-band tomograms obtained with the previously described BF estimator. The RH99 and RH50 relative height metrics are shown overplotted to the tomograms and considered as a reference.

Fig. 10(a) and (b) displays the tomographic profiles obtained after the phase calibration operation utilizing disjoint estimation with reference to SM configuration [Fig. 6(a)] and MM sequential pairing configuration [see topology depicted in green in Fig. 6(b)], respectively. Fig. 10(d) shows the profile achieved by joint estimation with the MM network obtained by pairing distances 1, 2, and 3 [see Fig. 6(b)]. It is rather evident how the proposed joint estimation provides a focusing characterized by a reduced level of sidelobes and generally a higher contrast, especially noticeable in the left region of the plots corresponding to the near range highlighted by the yellow box in Fig. 10. As for the disjoint estimation, the sidelobe reduction achieved by the MM sequential pairing in Fig.10(b) is in fact higher than that of the SM case reported in Fig.10(a). Moreover, considering the near range, the sidelobe reduction for the joint approach in Fig.10(d) is even better than the disjoint estimation. Finally, the red level corresponding to the concentration of the scattering on the ground in the vegetation-free area, such as that corresponding to the yellow box at near range, is much more evident in Fig. 10(d) than in (b) (disjoint estimation).

At this point, one might wonder what happens when, similar to the joint estimation, an MM disjoint estimation is used with a network describing a paring with a higher

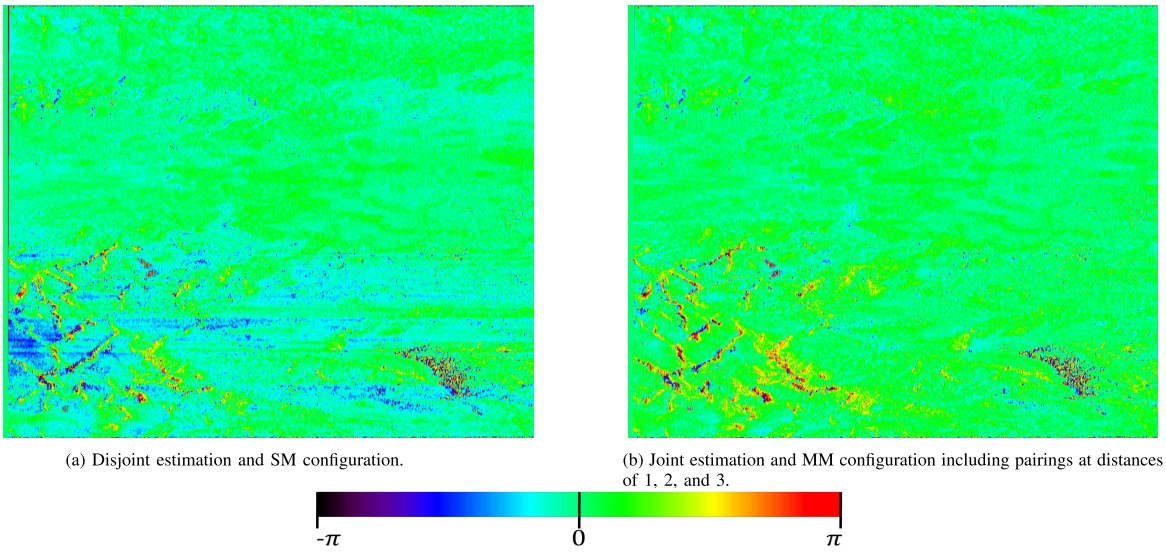

(a) Disjoint estimation and SM configuration.

(b) Joint estimation and MM configuration including pairings at distances of 1, 2, and 3.

Fig. 8. Compensated interferometric phase for the pair of acquisitions 5 and 6 obtained with: (a) classical (disjoint) and SM configuration and (b) proposed (joint) estimation approach and MM configuration.

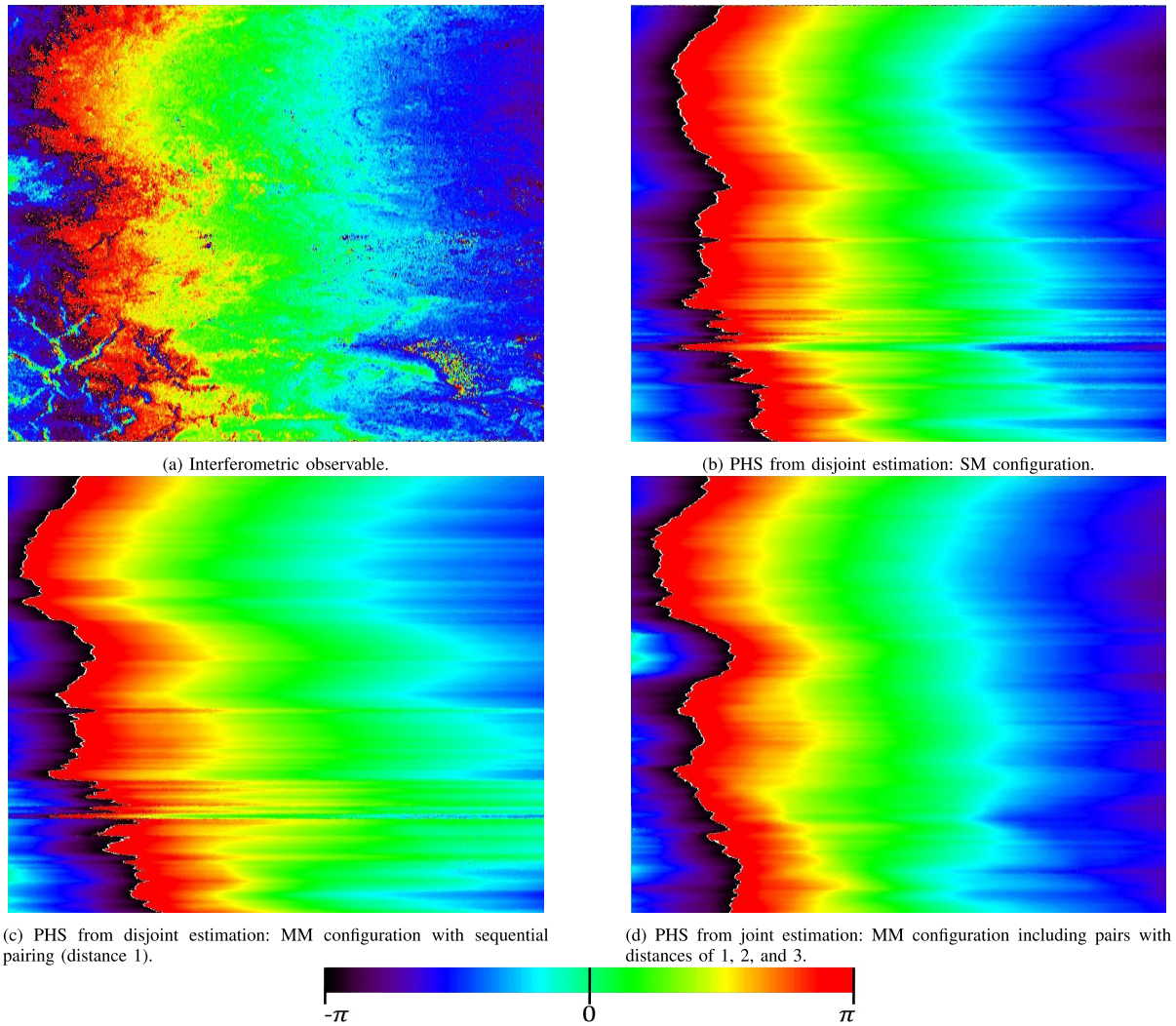

(a) Interferometric observable.

(b) PHS from disjoint estimation: SM configuration.

(c) PHS from disjoint estimation: MM configuration with sequential pairing (distance 1).

(d) PHS from joint estimation: MM configuration including pairs with distances of 1, 2, and 3.

Fig. 9. Results obtained for the pair of acquisitions 6 and 8 (a) interferometric phase (observable) and corresponding phase screens (PHSs) reconstructed with the classical (disjoint) estimation approach, for (b) SM and (c) MM configurations, and with (d) proposed (joint) estimation approach for the MM configuration.

degree of connectivity. In Fig. 10(c), we show the case of a disjoint estimation with an MM configuration characterized by distances 1, 2, and 3 [Fig. 6(b)], i.e., the same configuration used for the generation of the joint estimation results

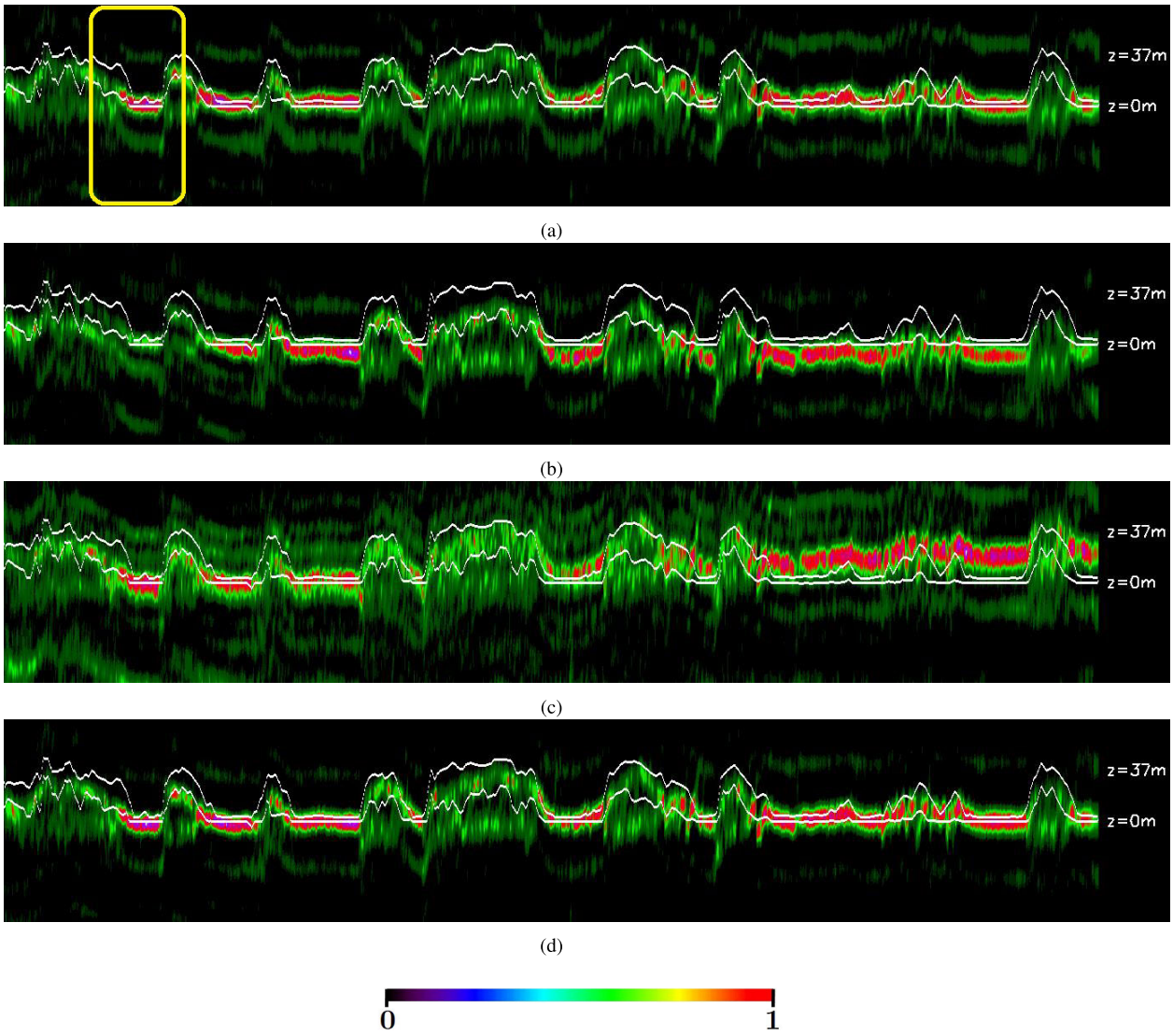

Fig. 10. Vertical (normalized) tomographic profile (−75, 75 m) along the range direction, corresponding to the horizontal white line in Fig. 4, obtained with phase calibration based on the classical (disjoint) and proposed (joint), with SM and MM configurations. The reference RH99 and RH50 metrics are overplotted (white lines) to the tomograms. (a) Disjoint estimation: SM configuration. (b) Disjoint estimation: MM configuration including pairs with distance 1 (sequential paring). (c) Disjoint estimation: MM configuration including pairs with distances 1 (sequential pairing) and 2 (i.e., a redundant interferogram network). (d) Joint estimation: MM configuration including pairs with distances 1 (sequential pairing), 2, and 3 (i.e., a redundant interferogram network).

of Fig. 10(d). In this case, it is evident—the strong reduction of performance of the phase calibration operation. This performance loss is due to the fact that the disjoint nonlinear optimization in (16) for an overcomplete set of interferometric combinations results in baseline error estimates that are mutually inconsistent. The estimated vectors $\delta\mathbf{u}_x$ and $\delta\mathbf{v}_x$ move outside the range of the linear operator $\mathbf{\Pi}_0$ in (9), and therefore, the recovery of the individual δS^n via (9) fails. In contrast, the joint estimation according to (19) directly recovers the individual δS^n without applying (9) at all. This result clearly demonstrates the relevance of the joint PHS estimation approach, which is the sole solution among those analyzed in this work that is able to cope with increased redundancy of the input MM data stack, associated with a higher degree of connectivity of the selected MM network.

Finally, to complete the analysis, in Fig. 11 the tomographic profiles along the azimuth direction are depicted, including those obtained with the disjoint estimation with (a) SM configuration, (b) MM configuration, and (c) the joint estimation with MM configuration. These results confirm that the approach based on joint estimation achieves a tomographic profile characterized by reduced sidelobe levels, and generally much higher quality compared to those pertinent to the disjoint estimation. The comparison between the different vertical profiles of Fig. 11 highlights the presence of vertical shifts, which may vary among the different strategies. Such rigid shifts result from the correlation between the estimated phase corrections and the baseline distribution. It is rather evident that the MM disjoint estimation with sequential pairing in Fig. 11(b) shows larger vertical shifts. This is possibly due to the integration operation of the estimated phase screens at the inversion stage in (11). The SM configuration in Fig. 11(a), which avoids such integration, seems less impaired by vertical shifts. Strategies suggested in [25] could be however investigated to constrain

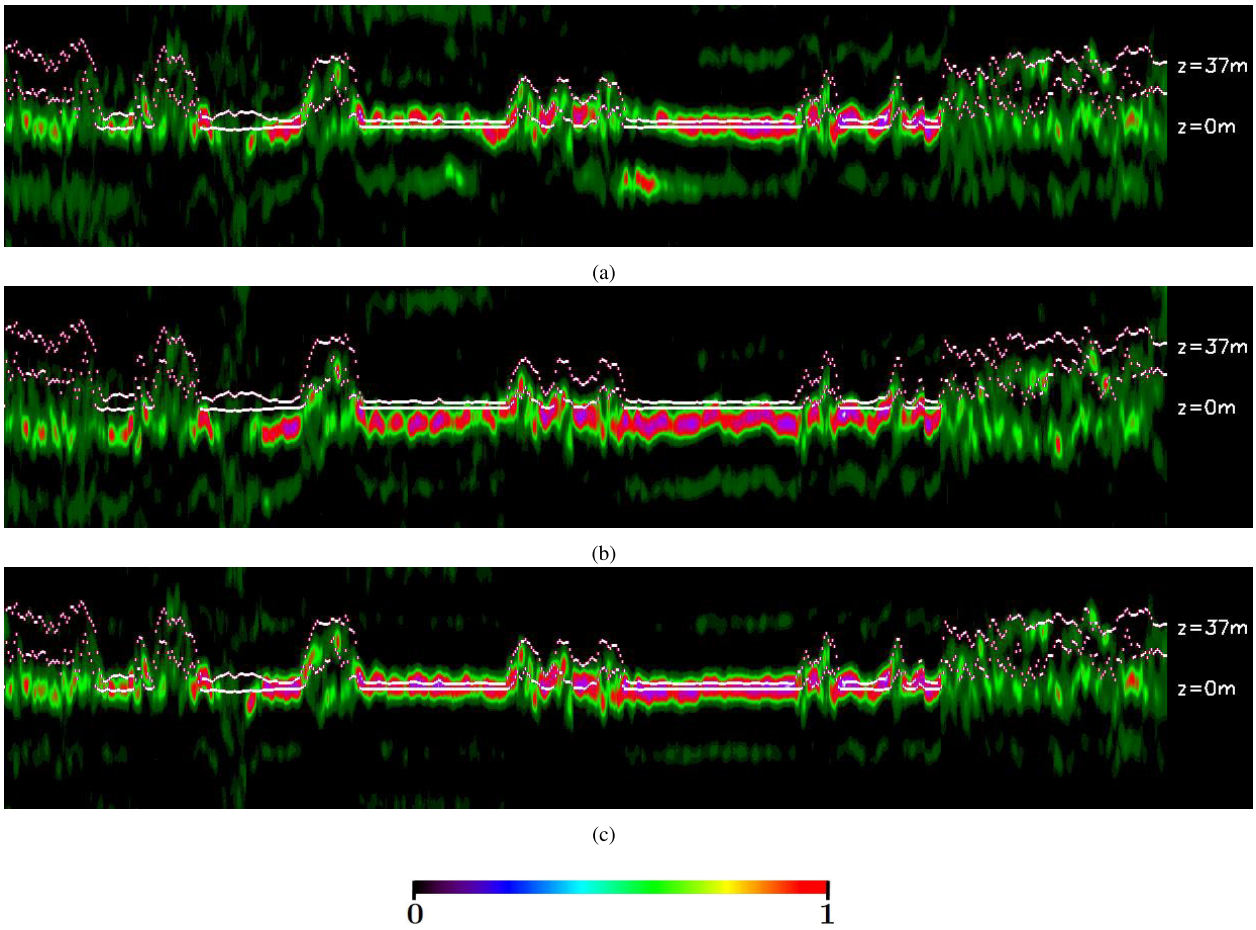

Fig. 11. Vertical (normalized) tomographic profile (−75, 75 m) along the azimuth direction, corresponding to the vertical white line in Fig. 4, obtained with phase calibration based on the classical (disjoint) and proposed (joint), with SM and MM configurations. The reference RH99 and RH50 metrics are overplotted (white lines) to the tomograms. (a) Disjoint estimation: SM configuration. (b) Disjoint estimation: MM configuration including pairs with distance 1 (sequential paring). (c) Joint estimation: MM configuration including pairs with distances 1 (sequential pairing), 2, and 3 (i.e., a redundant interferogram network).

the phase-screen solution to be orthogonal to the baseline distribution, thus achieving a vertical lock.

V. Further Discussions

So far, in addition to the introduction and motivation of the work, the proposed method for the phase calibration of MB data has been described and its effectiveness on real SAR data has been shown. Comments on the assumptions and choices made in the implementation of the methodology are now in order.

First, to enhance the robustness of the methods and simultaneously achieve a well-balanced gridding, we primarily performed a multilook operation on the interferograms, implemented mainly along the azimuth direction. Second, no constraints on the trajectory deviations to be retrieved have been imposed during the inversion process. More precisely, the solution to the problems in (15) and (18) has been obtained without enforcing any continuity requirements along the azimuth direction that would be associated with the typical dynamic of residual deviations of the aircraft. This choice has been dictated from the need to show the performance achieved by both classical and proposed methods using unconstrained optimization formulations. Obviously, possible limitations to the class of achievable solutions, dictated by the dynamic of the motion errors, can be integrated in both the proposed and classical methods. It is also clear that increasing the number of looks along the azimuth direction inherently provides smoother solutions.

Third, one might wonder the rationale behind opting for the generation of vertical profiles through classical Fourier BF. Indeed, advanced tomographic focusing methods such as Capon or MUSIC could have been used to achieve enhanced sidelobe suppression. Nonetheless, enhancements attained through these methods come at the cost of introducing radiometric distortions during the inversion process for estimating the vertical scattering profile. Furthermore, in our case, improvements in the data calibration process could have been masked out in the final results. Regardless of the implemented focusing method (BF or Capon), starting from a more accurately calibrated product is undeniably an advantage for enhancing the overall quality of the final vertical profiles. Finally, we did not implement any double localization as well as any phase triangulation procedure, as those proposed in [8], [36]. As for the double-localization procedure, it should be noted that it presumes the implementation of an iterative

approach in which the processing here described constitutes the first stage of the iteration, followed by a vertical peak extraction in each (horizontal) pixel. From Fig. 10, it should be clear that higher peak-to-sidelobe ratio levels, as those achieved in Fig. 10(d), should be in any case beneficial also for the application of the mentioned double-localization approach. The choice to avoid the phase triangulation is conservative, and related to the need of testing the estimation algorithm for data directly associated to a distributed scattering corresponding to a vegetated area.

VI. Conclusion

In this article, we have introduced a novel method for phase-screen estimation and compensation in airborne multibaseline TomoSAR data processing.

Having a robust calibration procedure is crucial for ensuring high-quality airborne tomographic results, given the challenges associated with the lack of accuracy in current navigation systems in guaranteeing sensor positions along all trajectories within a small fraction of the wavelength.

We have proposed an innovative approach for the calibration of multibaseline airbone SAR data stacks based on a joint estimation of the phase screens induced by residual trajectory deviations. The effectiveness of the proposed method has been experimentally demonstrated by using P-band airborne SAR data stacks acquired in the frame of the AfriSAR measurement campaign. Future studies will also be dedicated to better investigate the computational complexity of the presented method and to develop an inherent computationally efficient implementation by using parallel processing [46]. The framework adopted in this study considers the joint processing of multibaseline data. Phase screens are estimated by minimizing, jointly, the residual phase on a set of interferograms. The solution is amenable to an extension toward the optimization of a cost function including indexes of quality of the tomographic profiles, like contrast or entropy, which are also effective in the presence of a distributed scattering corresponding to vegetated areas.

References

[1] A. Reigber and A. Moreira, "First demonstration of airborne SAR tomography using multibaseline L-band data," *IEEE Trans. Geosci. Remote Sens.*, vol. 38, no. 5, pp. 2142–2152, Sep. 2000.

[2] M. Tello, V. Cazcarra-Bes, M. Pardini, and K. Papathanassiou, "Forest structure characterization from SAR tomography at L-band," *IEEE J. Sel. Topics Appl. Earth Observ. Remote Sens.*, vol. 11, no. 10, pp. 3402–3414, Oct. 2018.

[3] H. Aghababaei et al., "Forest SAR tomography: Principles and applications," *IEEE Geosci. Remote Sens. Mag.*, vol. 8, no. 2, pp. 30–45, Jun. 2020.

[4] G. Fornaro, A. Pauciullo, V. Pascazio, G. Schirinzi, and D. Reale, *Multi-Dimensional Imaging With Synthetic Aperture Radar*. Amsterdam, The Netherlands: Elsevier, 2024.

[5] G. Fornaro, F. Lombardini, and F. Serafino, "Three-dimensional multipass SAR focusing: Experiments with long-term spaceborne data," *IEEE Trans. Geosci. Remote Sens.*, vol. 43, no. 4, pp. 702–714, Apr. 2005.

[6] G. Fornaro, F. Serafino, and D. Reale, "4-D SAR imaging: The case study of Rome," *IEEE Geosci. Remote Sens. Lett.*, vol. 7, no. 2, pp. 236–240, Apr. 2010.

[7] D. Reale, G. Fornaro, A. Pauciullo, X. Zhu, and R. Bamler, "Tomographic imaging and monitoring of buildings with very high resolution SAR data," *IEEE Geosci. Remote Sens. Lett.*, vol. 8, no. 4, pp. 661–665, Jul. 2011.

[8] S. Tebaldini, F. Rocca, M. M. d'Alessandro, and L. Ferro-Famil, "Phase calibration of airborne tomographic SAR data via phase center double localization," *IEEE Trans. Geosci. Remote Sens.*, vol. 54, no. 3, pp. 1775–1792, Mar. 2016.

[9] S. Tebaldini and F. Rocca, "Multibaseline polarimetric SAR tomography of a boreal forest at P- and L-bands," *IEEE Trans. Geosci. Remote Sens.*, vol. 50, no. 1, pp. 232–246, Jan. 2012.

[10] O. Frey and E. Meier, "3-D time-domain SAR imaging of a forest using airborne multibaseline data at L- and P-bands," *IEEE Trans. Geosci. Remote Sens.*, vol. 49, no. 10, pp. 3660–3664, Oct. 2011.

[11] M. Lavalle and S. Hensley, "Extraction of structural and dynamic properties of forests from polarimetric-interferometric SAR data affected by temporal decorrelation," *IEEE Trans. Geosci. Remote Sens.*, vol. 53, no. 9, pp. 4752–4767, Sep. 2015.

[12] T. Le Toan et al., "The BIOMASS mission: Mapping global forest biomass to better understand the terrestrial carbon cycle," *Remote Sens. Environ.*, vol. 115, no. 11, pp. 2850–2860, Nov. 2011.

[13] M. L. Imhoff, "Radar backscatter and biomass saturation: Ramifications for global biomass inventory," *IEEE Trans. Geosci. Remote Sens.*, vol. 33, no. 2, pp. 511–518, Mar. 1995.

[14] Y. Yu and S. Saatchi, "Sensitivity of L-band SAR backscatter to aboveground biomass of global forests," *Remote Sens.*, vol. 8, no. 6, p. 522, Jun. 2016.

[15] G. Fornaro, G. Franceschetti, and S. Perna, "Motion compensation errors: Effects on the accuracy of airborne SAR images," *IEEE Trans. Aerosp. Electron. Syst.*, vol. 41, no. 4, pp. 1338–1352, Oct. 2005.

[16] I. El Moussawi et al., "L-band UAVSAR tomographic imaging in dense forests: Gabon forests," *Remote Sens.*, vol. 11, no. 5, p. 475, Feb. 2019.

[17] P. C. Dubois-Fernandez et al., "The TropiSAR airborne campaign in French Guiana: Objectives, description, and observed temporal behavior of the backscatter signal," *IEEE Trans. Geosci. Remote Sens.*, vol. 50, no. 8, pp. 3228–3241, Aug. 2012.

[18] M. Lavalle, B. Hawkins, and S. Hensley, "Tomographic imaging with UAVSAR: Current status and new results from the 2016 AfriSAR campaign," in *Proc. IEEE Int. Geosci. Remote Sens. Symp. (IGARSS)*, Jul. 2017, pp. 2485–2488.

[19] M. Mariotti D'Alessandro and S. Tebaldini, "Digital terrain model retrieval in tropical forests through P-band SAR tomography," *IEEE Trans. Geosci. Remote Sens.*, vol. 57, no. 9, pp. 6774–6781, Sep. 2019.

[20] S. Tebaldini, "Algebraic synthesis of forest scenarios from multibaseline PolInSAR data," *IEEE Trans. Geosci. Remote Sens.*, vol. 47, no. 12, pp. 4132–4142, Dec. 2009.

[21] A. Pepe, P. Berardino, M. Bonano, L. D. Euillades, R. Lanari, and E. Sansosti, "SBAS-based satellite orbit correction for the generation of DInSAR time-series: Application to RADARSAT-1 data," *IEEE Trans. Geosci. Remote Sens.*, vol. 49, no. 12, pp. 5150–5165, Dec. 2011.

[22] A. Moreira and Y. Huang, "Airborne SAR processing of highly squinted data using a chirp scaling approach with integrated motion compensation," *IEEE Trans. Geosci. Remote Sens.*, vol. 32, no. 5, pp. 1029–1040, Sep. 1994.

[23] G. Fornado, "Trajectory deviations in airborne SAR: Analysis and compensation," *IEEE Trans. Aerosp. Electron. Syst.*, vol. 35, no. 3, pp. 997–1009, Jul. 1999.

[24] M. Pardini, K. Papathanassiou, V. Bianco, and A. Iodice, "Phase calibration of multibaseline SAR data based on a minimum entropy criterion," in *Proc. IEEE Int. Geosci. Remote Sens. Symp.*, Jul. 2012, pp. 5198–5201.

[25] H. Aghababaee, G. Fornaro, and G. Schirinzi, "Phase calibration based on phase derivative constrained optimization in multibaseline SAR tomography," *IEEE Trans. Geosci. Remote Sens.*, vol. 56, no. 11, pp. 6779–6791, Nov. 2018.

[26] G. Fornaro and P. Imperatore, "Airborne P-band SAR tomography over lop tropical forest based on joint estimation of multibaseline phase-screens," in *Proc. IEEE Int. Geosci. Remote Sens. Symp. (IGARSS)*, Jun. 2024.

[27] I. Hajnsek et al., "SAR imaging of tropical African forests with P-band multibaseline acquisitions: Results from the AfriSAR campaign," in *Proc. IEEE Int. Geosci. Remote Sens. Symp. (IGARSS)*, Jul. 2016, pp. 7521–7523.

[28] P. Berardino, G. Fornaro, R. Lanari, and E. Sansosti, "A new algorithm for surface deformation monitoring based on small baseline differential SAR interferograms," *IEEE Trans. Geosci. Remote Sens.*, vol. 40, no. 11, pp. 2375–2383, Nov. 2002.

[29] N. Ge, R. Bamler, D. Hong, and X. X. Zhu, "Single-look multi-master SAR tomography: An introduction," *IEEE Trans. Geosci. Remote Sens.*, vol. 59, no. 3, pp. 2132–2154, Mar. 2021.

[30] L. J. Grady and J. R. Polimeni, *Discrete Calculus: Applied Analysis on Graphs for Computational Science*, vol. 3. Cham, Switzerland: Springer, 2010.

[31] N. Biggs, *Algebraic Graph Theory*, no. 67. Cambridge, U.K.: Cambridge Univ. Press, 1993.

[32] P. Imperatore, A. Pepe, and R. Lanari, "Multichannel phase unwrapping: Problem topology and dual-level parallel computational model," *IEEE Trans. Geosci. Remote Sens.*, vol. 53, no. 10, pp. 5774–5793, Oct. 2015.

[33] F. R. Chung, *Spectral Graph Theory*, vol. 92. Providence, RI, USA: American Mathematical Society, 1997.

[34] A. De Maio, G. Fornaro, and A. Pauciullo, "Detection of single scatterers in multidimensional SAR imaging," *IEEE Trans. Geosci. Remote Sens.*, vol. 47, no. 7, pp. 2284–2297, Jul. 2009.

[35] A. Ferretti, A. Fumagalli, F. Novali, C. Prati, F. Rocca, and A. Rucci, "A new algorithm for processing interferometric data-stacks: SqueeSAR," *IEEE Trans. Geosci. Remote Sens.*, vol. 49, no. 9, pp. 3460–3470, Sep. 2011.

[36] G. Fornaro, S. Verde, D. Reale, and A. Pauciullo, "CAESAR: An approach based on covariance matrix decomposition to improve multibaseline–multitemporal interferometric SAR processing," *IEEE Trans. Geosci. Remote Sens.*, vol. 53, no. 4, pp. 2050–2065, Apr. 2015.

[37] P. Stoica and R. L. Moses, *Spectral Analysis of Signals*, vol. 452. Upper Saddle River, NJ, USA: Prentice-Hall, 2005.

[38] J. Capon, "High-resolution frequency-wavenumber spectrum analysis," *Proc. IEEE*, vol. 57, no. 8, pp. 1408–1418, Jan. 1969.

[39] T. Marzetta, "A new interpretation of Capon's maximum likelihood method of frequency-wavenumber spectral estimation," *IEEE Trans. Acoust., Speech, Signal Process.*, vol. ASSP-31, no. 2, pp. 445–449, Apr. 1983.

[40] T. Fatoyinbo et al., "The NASA AfriSAR campaign: Airborne SAR and LiDAR measurements of tropical forest structure and biomass in support of current and future space missions," *Remote Sens. Environ.*, vol. 264, Oct. 2021, Art. no. 112533.

[41] P. Imperatore, "SAR imaging distortions induced by topography: A compact analytical formulation for radiometric calibration," *Remote Sens.*, vol. 13, no. 16, p. 3318, 2021.

[42] L. M. H. Ulander, "Radiometric slope correction of synthetic-aperture radar images," *IEEE Trans. Geosci. Remote Sens.*, vol. 34, no. 5, pp. 1115–1122, Sep. 1996.

[43] I. Hajnsek, M. Pardini, M. Jger, R. Horn, J. S. Kimn, and K. P. H. Jrg, "Technical assistance for the development of airborne SAR and geophysical measurements during the AfriSAR campaign—Deliverable DD-4 final report," Eur. Space Agency (ESA), Paris, France, Tech. Rep., 2017.

[44] *Lvis Mission LiDAR Data*, NASA/ESA/DLR/AGEOS Afrisar Campaign. [Online]. Available: https://lvis.gsfc.nasa.gov/Data/Maps/Gabon2016Map.html

[45] J. Armston et al. (2020). *Afrisar: Gridded Forest Biomass and Canopy Metrics Derived From Lvis, Gabon, 2016*. [Online]. Available: https://daac.ornl.gov/cgi-bin/dsviewer.pl?ds_id=1775

[46] P. Imperatore, A. Pepe, and E. Sansosti, "High performance computing in satellite SAR interferometry: A critical perspective," *Remote Sens.*, vol. 13, no. 23, p. 4756, Nov. 2021.

Pasquale Imperatore (Senior Member, IEEE) received the Laurea degree (summa cum laude) in electronic engineering and the Ph.D. degree in electronic and telecommunication engineering, from the University of Naples Federico II, Naples, Italy, in 2001 and 2010, respectively.

He is currently a Research Scientist at National Research Council (CNR), Institute for Electromagnetic Sensing of the Environment (IREA), Naples. Previously, he worked with Wise S.p.A., Naples, and later with CREATE-NET, Trento, Italy. Subsequently, he joined the Department of Biomedical, Electronic, and Telecommunication Engineering at the University of Naples Federico II. His research interests include microwave remote sensing and electromagnetic propagation and scattering, with particular emphasis on theoretical scattering models, waves in random layered media, synthetic aperture radar (SAR) data modeling, processing, and calibration, SAR interferometry, parallel algorithms, and high-performance computing (HPC). He has authored or coauthored numerous research articles in peer-reviewed journals, book chapters, and conference proceeding.

Dr. Imperatore is a member of the Topical Advisory Panel for Geomatics (MDPI) and the Earth and Planetary Science Scientific Advisory Board for IntechOpen. He served as the lead editor for several journal special issues and as a reviewer for numerous peer-reviewed journals. He is an Associate Editor for IEEE GEOSCIENCE AND REMOTE SENSING LETTERS and an Associate Editor for *Frontiers in Imaging*. Moreover, he has coedited two books in the field of remote sensing and geospatial technology.

Gianfranco Fornaro (Fellow, IEEE) received the M.S. degree (summa cum laude) in electronic engineering and the Ph.D. degree from the University of Naples Federico II, Naples, Italy, in 1992 and 1997, respectively.

Since 1993, he has been with IREA-CNR, Naples, where he is currently the Research Director working in the area of synthetic aperture radar (SAR) remote sensing. He was an Adjunct Professor of telecommunications in several universities in South Italy. In 2013, he achieved the Full Professor Habilitation in the telecommunication area. Since 2010, he has been a Lecturer at the International Summer School on Radar/SAR organized by the Fraunhofer FHR Institute, Bonn, Germany. From 2013 to 2018, he was a Lecturer at the NATO Lecture Series SET 191 and SET 235. He is the author of the book *Multi-Dimensional Imaging with Synthetic Aperture Radar* (Elsevier).

Dr. Fornaro received the Mountbatten Premium by the IEE Society in 1997, the 2011 IEEE GRSL Best Paper Award, and the 2011 Best Reviewers Mention of IEEE TRANSACTIONS ON GEOSCIENCE AND REMOTE SENSING journal. He was a Guest Editor of *EURASIP Journal on Advances in Signal Processing* and *IEEE Signal Processing Magazine*. He is an Associate Editor of IEEE GEOSCIENCE REMOTE SENSING LETTERS (GRSL).

Open Access funding provided by 'Consiglio Nazionale delle Ricerche-CARI-CARE-ITALY' within the CRUI CARE Agreement